Monthly Notices of the ROYAL ASTRONOMICAL SOCIETY

MNRAS **503,** 2523–2538 (2021) doi:10.1093/mnras/stab464

Correlations between γ-ray luminosity and magnetization of the jet as well as relativistic electron injection power: cases for Mrk 421, 3C 454.3 and 3C 279

Wen Hu [1]★ Dahai Yan [2]★ and Qianglin Hu [1]

[1]*Department of Physics, Jinggangshan University, Jiangxi Province, Ji'an 343009, China*

[2]*Key Laboratory for the Structure and Evolution of Celestial Objects, Yunnan Observatories, Chinese Academy of Sciences, Kunming 650011, China*

Accepted 2021 February 12. Received 2021 February 11; in original form 2020 November 19

ABSTRACT

By fitting high-quality and simultaneous multiwavelength spectral energy distributions at multiple epochs with a one-zone leptonic jet model, we study the jet properties of three famous blazars: Mrk 421, 3C 454.3 and 3C 279. In the jet model, the emitting electron energy distributions are calculated by solving the kinetic equations of electron injection, escape, adiabatic and radiative energy losses. To explore multidimensional parameter space systematically, we employ a Markov chain Monte Carlo fitting technique. The properties of the emission regions we have derived here are consistent with those in previous studies, for example, the particle-dominated and low-magnetization jet. The new finding is that there is a tight correlation between γ-ray luminosity and electron injection power and an anticorrelation between γ-ray luminosity and the jet magnetization parameter. The results suggest that the same energy-dissipative mechanism (such as a shock) could be operating in the jets of different types of blazars, and that the origin of γ-ray flares is associated with the particle acceleration process.

Key words: radiation mechanisms: non-thermal – galaxies: active – galaxies: individual: Mrk 421 – galaxies: individual: 3C 454.3 – galaxies: individual: 3C 279 – galaxies: jets.

1 INTRODUCTION

Flat spectrum radio quasars (FSRQs) and BL Lacertae objects (BL Lacs) constitute a subset of active galactic nuclei (AGNs), which are called blazars. A blazar is characterized by flux variability at all wavelengths, high polarization at optical and radio frequencies (e.g. D'arcangelo et al. 2009; Marscher et al. 2010; Peceur, Tayler & Kraan-Korteweg 2020), apparently superluminal jet components (e.g. Jorstad et al. 2004, 2005; Homan et al. 2009), and non-thermal emission from a relativistic jet pointed close to the observer's line of sight (Urry & Padovani 1995).

Compared with BL Lacs that have featureless optical spectra, FSRQs display prominent emission lines with the equivalent width ≥ 5Å and the prominent ultraviolet excess, which is attributed to the thermal emission of the accretion disc (Urry & Padovani 1995). The multiwavelength (MWL) spectral energy distribution (SED) of a blazar is characterized by two prominent peaks. The first peak, which is attributed to the synchrotron emission of high-energy electrons in the jet, is generally located at infrared/optical bands. The second peak, which could be generated by inverse Compton (IC) scattering off low-energy photons by high-energy electrons, is generally located at γ-ray energies. The low photon fields for the IC scattering can include synchrotron emission from the high-energy electrons themselves, called synchrotron self-Compton (SSC) scattering (Bloom & Marscher 1996; Finke, Dermer & Böttcher 2008), and external photon fields surrounding the jet, called external Compton (EC) scattering. Depending on the location of the emission region, the external photon field responsible for the EC emission could be either from the dusty torus (DT; Blazejowski et al. 2000; Dermer et al. 2014; Yan, Zhang & Zhang 2015; Hu et al. 2017; Wu et al. 2018), and/or from the broad-line region (BLR; Sikora, Begelman & Rees 1994; Yan, Zeng & Zhang 2012; Böttcher et al. 2013; Hu, Fan & Dai 2015).

Electron acceleration in a blazar jet is still an open question. In general, it can be achieved by the energy dissipated in shocks and/or magnetic reconnections. If the jet is dominated by the kinetic energy flux at the dissipation distance, then shocks are natural candidates for powering the jet emission and accelerating electrons to ultrarelativistic energy (Marscher & Gear 1985; Kirk et al. 2000; Spada et al. 2001; Sironi & Spitkovsky 2009; Summerlin & Baring 2012). The shock scenario is supported by multiple observations of γ-ray outbursts in coincidence with the emergence of a jet perturbation in or close to the radio core of blazars (e.g. Marscher et al. 2008; Jorstad et al. 2013; Abeysekara et al. 2018). If the jet remains Poynting flux-dominated at the energy dissipation distance, then shocks are generally expected to be weak, and magnetic reconnection is a more plausible candidate for the acceleration of electrons (e.g. Cerutti, Uzdensky & Begelman 2012; Sironi, Spitkovsky & Arons 2013; Sironi & Spitkovsky 2014; Guo et al. 2014, 2015). The ratio between the Poynting flux and kinetic energy flux, namely the

★ E-mail: huwen.3000@jgsu.edu.cn (WH); yandahai@ynao.ac.cn (DY)

magnetization parameter $\sigma_{\rm m} \equiv B'^2/4\pi\rho' c^2$, is a crucial quantity to discriminate between the two scenarios.[1]

Recently, particle-in-cell (PIC) simulations of relativistic magnetic reconnection have demonstrated that electrons can be efficiently accelerated to form a non-thermal distribution for $\sigma_{\rm m} \gtrsim 1$ (see Petropoulou et al. 2019, and references therein). The magnetic reconnection scenario has been proposed to account for many of the extreme spectral and temporal properties of blazars (Giannios, Uzdensky & Begelman 2009; Giannios 2013; Petropoulou, Giannios & Sironi 2016; Christie et al. 2019). The magnetic reconnection scenario predicts a near equipartition between the energies carried by the magnetic field and emitting electrons (Sironi, Petropoulou & Giannios 2015; Petropoulou et al. 2019).

Modelling the broad-band SED of a blazar is frequently used to probe blazar jet physics (e.g. Ghisellini et al. 2010; Yan et al. 2013; Yan, Zeng & Zhang 2014; Ghisellini & Tavecchio 2015; Inoue & Tanaka 2016; Chen 2018). Because blazar emission often shows strong variabilities at all wavelengths, the evolution of well-sampled simultaneous SEDs at different epochs is important. In this work, we investigate the jet physics in three typical blazars (3C 454.3, Mrk 421 and 3C 279) by modelling their quasi-simultaneous SEDs in multiple activity states.

The outline of this paper is as follows. Section 2 describes the jet model and the fitting method. In Section 3, we report our results. Finally, in Section 4, we discuss our results and summarize our conclusions. Throughout the paper, we use a flat cosmology model with the following parameters: $\rm H_0 = 70\ km\ s^{-1}\ Mpc^{-1}$, $\Omega_{\rm M} = 0.3$ and $\Omega_\Lambda = 0.7$ (Hinshaw et al. 2013; Bennett et al. 2013).

2 MODEL

We adopt a one-zone homogeneous leptonic jet model. It is assumed that emissions are produced in a spherical blob of radius R', which moves relativistically with the bulk Lorentz factor Γ in the observer's frame at an angle $\theta_{\rm obs} \sim \Gamma^{-1}$ with respect to our line of sight. The emission region is filled with a uniform and tangled magnetic field of strength B'. The radius of the emission region is estimated from the minimum variability time-scale $t_{\rm var}$, through $R' = c\,\delta_{\rm D} t_{\rm var}/(1+z)$, where z is the redshift of the source and the Doppler factor $\delta_{\rm D}$ is approximated as Γ. Throughout this paper, all primed quantities refer to the comoving frame of the emission region and unprimed quantities denote the observer's frame.

It is assumed that a population of ultrarelativistic non-thermal electrons is continuously injected into the blob with a rate of $Q'_{\rm e}(\gamma')$ in units of $\rm s^{-1}$. The injected electrons lose energy through radiation and adiabatic processes. The kinetic equation that governs the evolution of electrons can be described by the time-dependent Fokker–Planck equation (Coppi & Blandford 1990; Chiaberge & Ghisellini 1999).

With respect to our previous work, we further refine the model, including a physically realistic, stratified BLR model proposed by Finke (2016). A modification is including adiabatic expansion, which may be important in modelling the SEDs of blazars (e.g. Lewis, Becker & Finke 2016; Lewis, Finke & Becker 2018). The radiation cooling from both EC–BLR and EC–DT processes is considered to calculate the radiating electron distribution.

We consider a single power law of electron injection, which is given by

$$\gamma'^2 Q'_{\rm e}(\gamma') = Q_0 \gamma'^{2-n}, \qquad \gamma'_{\rm min} \le \gamma' \le \gamma'_{\rm max}, \tag{1}$$

with

$$Q'_0 = \begin{cases} \dfrac{L'_{\rm inj}}{m_{\rm e}c^2} \dfrac{2-n}{\gamma'^{\,2-n}_{\rm max} - \gamma'^{\,2-n}_{\rm min}}; & n \neq 2 \\ \dfrac{L'_{\rm inj}}{m_{\rm e}c^2 \ln(\gamma'_{\rm max}/\gamma'_{\rm min})}; & n = 2 \end{cases}, \tag{2}$$

where $\gamma'_{\rm min}$ and $\gamma'_{\rm max}$ are the low- and high-energy cut-offs, respectively, $L'_{\rm inj}$ is the injection power of electrons in units of erg $\rm s^{-1}$, n is the power-law index, $m_{\rm e}$ is the rest mass of an electron and c is the speed of light.

2.1 Emitting electron energy distribution

The kinetic equation governing the evolution of the electron energy distribution, $N'_{\rm e}(\gamma')$, is given by

$$\frac{\partial N'_{\rm e}(\gamma')}{\partial t'} = -\frac{\partial}{\partial \gamma'}\left[\dot{\gamma}' N'_{\rm e}(\gamma')\right] - \frac{N'_{\rm e}(\gamma')}{t'_{\rm esc}} + Q'_{\rm e}(\gamma'), \tag{3}$$

where $t'_{\rm esc}$ is the escape time-scale of electrons and $\dot{\gamma}'$ is the energy-loss rate of the electrons.

In a blazar jet, the electrons lose energy through synchrotron and IC scattering on internal and external photon fields. The external radiation fields surrounding the jet include BLR and DT photon fields. Therefore, the electron radiative cooling rate can be written as $\dot{\gamma}'_{\rm rad} = \dot{\gamma}'_{\rm syn} + \dot{\gamma}'_{\rm ssc} + \dot{\gamma}'_{\rm BLR} + \dot{\gamma}'_{\rm DT}$, where $\dot{\gamma}'_{\rm syn}$, $\dot{\gamma}'_{\rm ssc}$, $\dot{\gamma}'_{\rm BLR}$ and $\dot{\gamma}'_{\rm DT}$ are the cooling rate due to the synchrotron, SSC, EC–BLR and EC–DT radiation, respectively.

The synchrotron energy-loss rate is given by

$$-\dot{\gamma}'_{\rm syn} = \frac{4\sigma_{\rm T}}{3m_{\rm e}c} U'_B \gamma'^2, \tag{4}$$

where $U'_B = B'^2/8\pi$ is the magnetic field energy density.

The SSC energy-loss rate is given by

$$-\dot{\gamma}'_{\rm ssc} = \frac{4\sigma_{\rm T}}{3m_{\rm e}c}\gamma'^2 \int_0^\infty {\rm d}\epsilon' u'_{\rm syn}(\epsilon') f_{\rm kn}(\epsilon', \gamma'), \tag{5}$$

where $u'_{\rm syn}(\epsilon')$ is the spectral energy density of the synchrotron radiation, and

$$f_{\rm kn}(\epsilon', \gamma') = \frac{9}{16}\int_{\gamma'_1}^{\gamma'} {\rm d}\gamma'' F_{\rm c}(x,q)\frac{\gamma' - \gamma''}{\epsilon'^2 \gamma'^4}, \tag{6}$$

where the lower limit for the integration is

$$\gamma'_1 \simeq \gamma' + \epsilon' - \frac{4\gamma'^2\epsilon'}{1+4\gamma'\epsilon'}$$

and the kernal function is

$$F_{\rm c}(x,q) = \left[2q\ln q + q + 1 - 2q^2 + \frac{(xq)^2}{2(1+xq)}(1-q)\right] H\left[q; \frac{1}{4\gamma'^2}, 1\right], \tag{7}$$

(Jones 1968; Blumenthal & Gould 1970). Here, $H(x; a, b)$ is the Heaviside function defined as $H = 1$ if $a \le x \le b$, and $H = 0$ otherwise. In the equation, $x = 4\epsilon'\gamma'$, $q = (\epsilon'_\gamma/\gamma')/x(1 - \epsilon'_\gamma/\gamma')$, and the scattered photon energy is $\epsilon'_\gamma = \gamma' + \epsilon' - \gamma''$.

The EC–DT energy-loss rate is given by

$$-\dot{\gamma}'_{\rm ec} = \frac{4\sigma_{\rm T}}{3m_{\rm e}c}\gamma^2 \int_0^\infty {\rm d}\epsilon u_{\rm ext}(\epsilon) f_{\rm kn}(\epsilon, \gamma), \tag{8}$$

where the quantities $\gamma = \delta_{\rm D}\gamma'$ and ϵ refer to the stationary frame with respect to the black hole (BH), and $u_{\rm ext}(\epsilon)$ is the spectral energy

[1] Here, B' and ρ' are the magnetic field strength and the rest-mass density in the rest frame of the jet, respectively.

density of the external photon field. Here, the DT radiation is assumed to be described as a dilute blackbody spectrum with a peak frequency of $\nu_{\rm DT} = 3 \times 10^{13}$ Hz in the lab frame (e.g. Tavecchio & Ghisellini 2008; Ghisellini & Tavecchio 2009). The spectral energy density is given by

$$u_{\rm ext}(\epsilon) = \frac{15U_0}{(\pi\Theta)^4}\frac{\epsilon^3}{\exp(\epsilon/\Theta)-1}, \quad (9)$$

where $\Theta = h\nu_{\rm DT}/2.82m_ec^2$ and $U_0 \simeq 2.1 \times 10^{-4}$ erg cm^3 are the dimensionless temperature and energy density of the DT radiation field, respectively.

The EC–BLR loss rate is given by

$$\dot{\gamma}'_{\rm BLR} = -\frac{4\sigma_{\rm T}}{3m_ec}\gamma^2\sum_{i=1}^{n=26}\oint {\rm d}\Omega u_{\rm BLR}(R_{\rm loc},\epsilon_i,\Omega) f_{\rm kn}(\epsilon_i,\gamma), \quad (10)$$

where $R_{\rm loc}$ is the location of the emission region, ϵ_i is the dimensionless energy of the lines, n denotes the number of different lines in the BLR model, and

$$f_{\rm kn}(\epsilon,\gamma) = \frac{9}{32}\int_{\gamma_1}^{\gamma} {\rm d}\gamma'' F_{\rm c}(x,q)\frac{\gamma-\gamma''}{\epsilon^2\gamma^4}. \quad (11)$$

Here, $\gamma_1 \simeq \gamma + \epsilon - [(2\gamma\bar{\epsilon})/(1+2\bar{\epsilon})]$, and

$$F_{\rm c}(x,q) = \left[y + y^{-1} - \frac{2\epsilon_\gamma}{\gamma\bar{\epsilon}y} + \left(\frac{\epsilon_\gamma}{\gamma\bar{\epsilon}y}\right)^2\right] \times H[\epsilon_\gamma; \frac{\bar{\epsilon}}{2\gamma}, \frac{2\gamma\bar{\epsilon}}{1+2\bar{\epsilon}}], \quad (12)$$

where $y = 1 - (\epsilon_\gamma/\gamma)$, $\bar{\epsilon} = \gamma\epsilon(1-\mu\mu_{\rm obs})$ and $\epsilon_\gamma = \gamma + \epsilon - \gamma''$ (Dermer & Schlickeiser 1993; Dermer et al. 2009). In the calculation, we adopt a stratified BLR model, with 26 different lines emitting at different radii, in a spherical shell configuration (Finke 2016). In the model, the location and luminosities of the various lines are estimated by using empirical relations derived from reverberation mapping, when the disc luminosity $L_{\rm d}$ has been specified.

In addition to the radiative losses, electrons also lose energy through adiabatic expansion of the outflowing plasma blob. The adiabatic loss is evaluated through

$$-\dot{\gamma}'_{\rm adi} = \frac{3c}{R'\delta_{\rm D}}\gamma', \quad (13)$$

assuming a conical jet with opening angle $\theta_{\rm op} \sim 1/\Gamma$ (Böttcher et al. 2013).

Therefore, the total cooling rate for electrons is $\dot{\gamma}' = \dot{\gamma}'_{\rm adi} + \dot{\gamma}'_{\rm rad}$.

We parametrize the escape time-scale in terms of the light crossing time-scale as $t'_{\rm esc} = \eta R'/c$ with $\eta > 1$. Here, we adopt a typical value of $\eta = 10$ (Böttcher & Chiang 2002; Hu et al. 2020).

With the above information, equation (3) is numerically solved by using the full implicit scheme described by Graff et al. (2008) to calculate the steady-state EED. Subsequently, the observed SEDs of synchrotron and IC emissions are calculated by using the formulas in Finke et al. (2008) and Dermer et al. (2009). Here, the synchrotron self-absorption (SSA) process is considered (Rybicki & Lightman 1979; Crusius & Schlickeiser 1986). We also consider the contribution from an accretion disc following Dermer & Schlickeiser (2002), which is assumed to be a Shakura & Sunyaev (1973) disc.

In summary, the model is characterized by eight parameters: B', n, $t_{\rm var}$, $\delta_{\rm D}$, $L'_{\rm inj}$, $\gamma'_{\rm min}$, $\gamma'_{\rm max}$ and $R_{\rm loc}$.

2.2 Fitting methodology

By applying the model to the observed SED, the free parameters and their uncertainties are estimated by performing the Markov chain Monte Carlo (MCMC) fitting method, which is a powerful tool to explore the multidimensional parameter space in blazar science (Yan et al. 2013, 2015). Details on the MCMC technique can be found in Lewis & Bridle (2002), Yuan et al. (2011) and Liu et al. (2012).

3 RESULTS

We apply the model described in Section 2 to the well-sampled SEDs of three famous blazars: 3C 454.3, Mrk 421 and 3C 279. The results of the fits to the observed SEDs are shown in Figs 1–3. The corner plots of the free parameters are displayed in the left panels of Figs A1–A4 in Appendix A. The fitted parameter values are tabulated in Table 1. In the calculations, a relative systematic uncertainty of 5 per cent was added in quadrature to the statistical error of the infrared–optical–UV and X-ray data (Poole et al. 2008; Abdo et al. 2011b).

3.1 SED modelling

3.1.1 3C 454.3

3C 454.3 is the brightest γ-ray FSRQ with a redshift $z = 0.859$ (Jackson & Browne 1991). In recent years, the source has attracted much attention, because of its remarkably high activity over the entire electromagnetic spectrum (e.g. Villata et al. 2006; Raiteri et al. 2008; Vercellone et al. 2009, 2010, 2011; Abdo et al. 2011a; Shah et al. 2017) and its broken power-law γ-ray spectrum (Abdo et al. 2009). Here, we focus on a simultaneous MWL campaign organized during 2009 November and December. The MWL SEDs are collected from Bonnoli et al. (2011). In order to investigate the change of the parameters in different active states, we also model the SED at the lowest γ-ray state since the beginning of *Fermi* Large Area Telescope (LAT) observations.

The bolometric luminosity of the accretion disc $L_{\rm d}$ is 3×10^{46} erg s^{-1} (Raiteri et al. 2007), and the mass of the black hole $M_{\rm BH}$ is 5×10^8 M$_\odot$ (Bonnoli et al. 2011). To further reduce the number of model parameters, we take $t_{\rm var} = 6$ h, according to the analysis of γ-ray variability (Tavecchio et al. 2010; Jorstad et al. 2013). Thus, there are six free parameters in the model: B', $\delta_{\rm D}$, $L'_{\rm inj}$, $\gamma'_{\rm min}$, n and $R_{\rm loc}$. The best-fitting values of the parameters are summarized in Table 1.

From Fig. 1, we can see that the model provides satisfactory fits to six SEDs. In the states of November 27 and December 2 and 3, the γ-rays can be well interpreted as the superposition of EC–BLR and EC–DT radiation, while in the other states, the γ-rays are attributed to the EC–DT emission. The X-ray emission in the highest γ-ray flare is dominated by the EC–DT component. In the other five states, the X-ray emission is almost attributed to the SSC component only.

3.1.2 Mrk 421

Mrk 421 ($z = 0.031$) is the first established extragalactic TeV γ-ray blazar (Punch et al. 1992), and is categorized as a high-frequency-peaked BL Lac (HBL). Here we focus on an MWL campaign conducted during high activity in 2010 March. The observational data are taken from Aleksić et al. (2015). For comparison, the data from a 4.5-month long MWL campaign (Abdo et al. 2011b) are also included in this work, which provides an unprecedented, complete look at the quiescent SED for the source. In order to account for

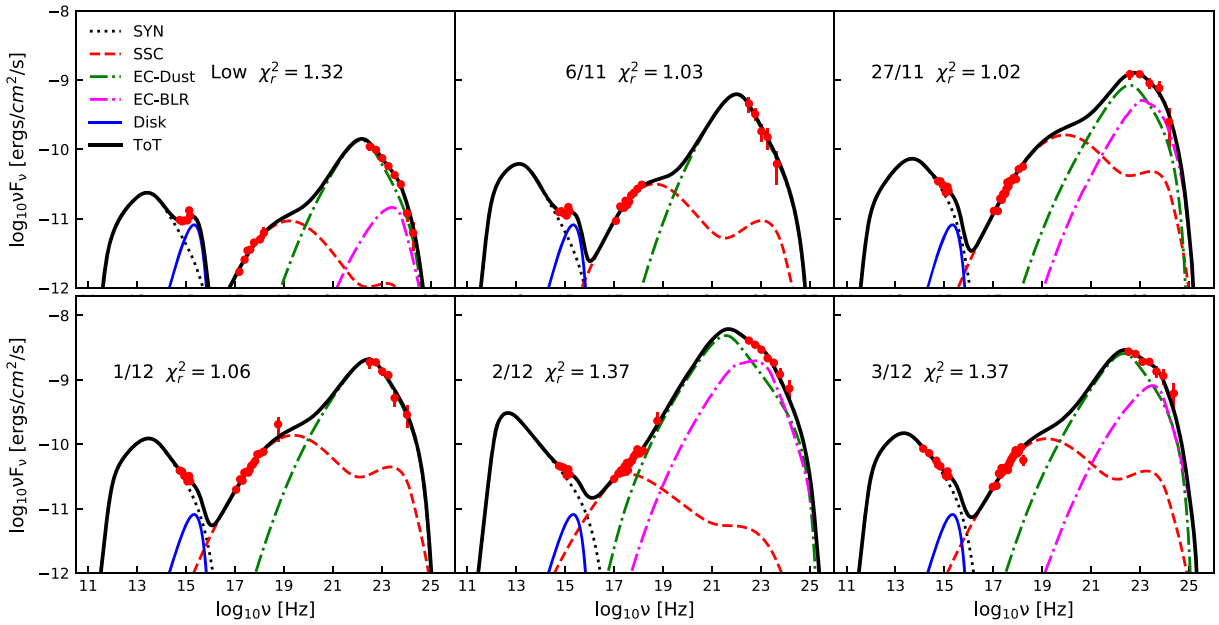

Figure 1. Comparisons of the best-fitting SEDs with observed data of 3C 454.3. The different components are labelled in the legend.

Table 1. Mean values and 1σ errors of the parameters for 3C 454.3, Mrk 421 and 3C 279. The † symbol denotes that the results were obtained with $t_{\rm var} = 1$ d.

State	B' (G)	$\delta_{\rm D}$	$\log_{10} L'_{\rm inj}$	$\log_{10} \gamma'_{\rm min}$	n	$\log_{10} R_{\rm loc}$	χ^2_r
3C 454.3							
Low	0.96 ± 0.22	30.90 ± 2.25	42.55 ± 0.09	2.80 ± 0.09	3.08 ± 0.35	–	1.32
Low†	0.70 ± 0.12	22.23 ± 1.69	43.14 ± 0.09	2.89 ± 0.12	2.90 ± 0.37	–	1.44
Nov 06	0.98 ± 0.21	37.39 ± 2.68	42.81 ± 0.07	2.63 ± 0.06	3.41 ± 0.32	–	1.03
Nov 27	0.60 ± 0.11	34.19 ± 2.70	43.35 ± 0.12	2.93 ± 0.12	2.63 ± 0.35	–	1.02
Dec 01	0.78 ± 0.10	40.44 ± 2.12	43.20 ± 0.06	2.81 ± 0.07	3.20 ± 0.23	–	1.06
Dec 02	1.04 ± 0.16	54.85 ± 4.52	43.13 ± 0.09	2.30 ± 0.14	3.06 ± 0.16	18.00 ± 0.06	1.37
Dec 03	0.74 ± 0.07	42.57 ± 2.20	43.28 ± 0.06	2.73 ± 0.08	3.01 ± 0.10	18.14 ± 0.14	1.37
Mrk 421							
Quiet	0.06 ± 0.01	59.86 ± 2.54	39.66 ± 0.01	2.88 ± 0.05	2.29 ± 0.04	5.65 ± 0.02	2.61
Quiet†	0.03 ± 0.003	23.54 ± 0.96	40.78 ± 0.03	3.20 ± 0.05	2.04 ± 0.04	6.02 ± 0.02	3.12
55266	0.03 ± 0.01	73.46 ± 6.04	39.60 ± 0.02	2.78 ± 0.08	2.11 ± 0.05	6.05 ± 0.02	2.47
55270	0.07 ± 0.02	54.25 ± 4.98	39.76 ± 0.04	2.82 ± 0.08	2.19 ± 0.07	5.75 ± 0.04	0.96
55277	0.13 ± 0.06	48.15 ± 9.78	39.68 ± 0.10	2.61 ± 0.15	2.05 ± 0.14	5.63 ± 0.07	1.15
3C 279							
Period A	1.28 ± 0.09	37.73 ± 1.12	41.85 ± 0.03	2.62 ± 0.02	3.68 ± 0.08	–	1.54
Period A†	0.98 ± 0.09	23.13 ± 0.79	42.80 ± 0.04	2.63 ± 0.04	3.62 ± 0.09	17.47 ± 0.10	0.80
Period C	1.13 ± 0.09	39.40 ± 1.12	42.08 ± 0.03	2.69 ± 0.02	3.58 ± 0.08	–	1.70
Period D	0.52 ± 0.06	42.86 ± 1.59	42.55 ± 0.06	2.98 ± 0.06	3.10 ± 0.10	–	1.54

the rapid variability, the minimum variability time-scale $t_{\rm var} = 1$ h is taken in the fittings (for a discussion, see Aleksić et al. 2015).

The best-fitting SEDs and observational data points are shown Fig. 2 and the obtained parameters are reported in Table 1. EC processes are neglected in the source. The radio data point from the Submillimeter Array (SMA) reported in Abdo et al. (2011b) is used to constrain $\gamma'_{\rm min}$ of the power-law electron injection. From Fig. 2, we can see that the fitting to each SED is successful.

3.1.3 3C 279

For comparison, we also revisit the jet properties of the famous FSRQ 3C 279 ($z = 0.538$), which was studied with a similar model in our previous work (Hu et al. 2020). Here, we focus on the results of an MWL observing campaign conducted during a phase of increased activity from 2013 December to 2014 April. The MWL SEDs are taken from Hayashida et al. (2015). In the fitting, we adopt $t_{\rm var} = 2$ h, which was obtained in period D in Hayashida et al. (2015). We adopt $L_{\rm d} = 2 \times 10^{45}$ erg s^{-1} (Pian et al. 1999) and $M_{\rm BH} = 5 \times 10^8\,{\rm M}_\odot$ (Gu, Cao & Jiang 2001; Woo & Urry 2002; Nilsson et al. 2009).

Fig. 3 shows the SED fitting results, with parameters summarized in Table 1. The SEDs can be fitted well by the model. During period A, we note that both the EC–DT and EC–BLR components are required to reproduce the γ-ray emission, while during period D, the γ-ray emission is dominated by the EC–DT component. During period C, an EC–BLR component is needed to account for the γ-ray emission. For all three states, the X-ray spectrum is attributed to SSC emission.

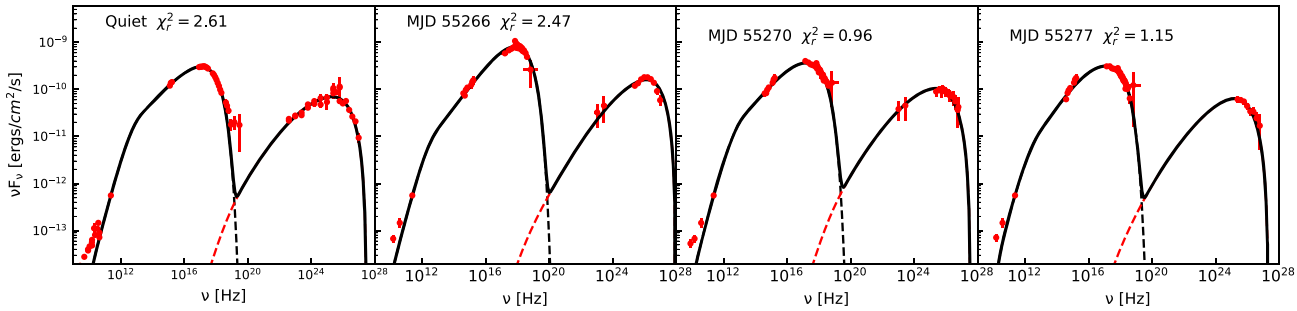

Figure 2. Comparisons of the best-fitting SEDs with observed data of Mrk 421. The black and red dashed lines refer to the synchrotron and SSC emission, respectively.

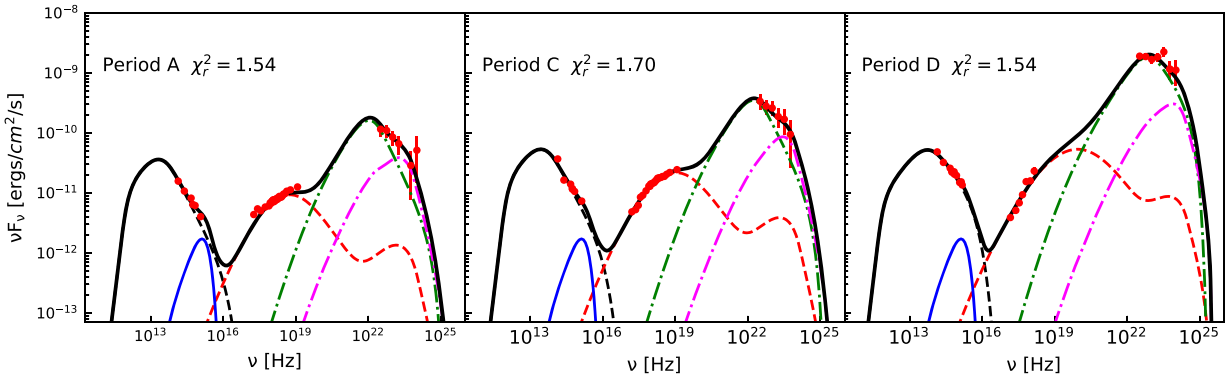

Figure 3. Comparisons of the best-fitting SEDs with observed data of 3C 279.

3.2 Physical properties of the jets

Evolution of model parameters could allow us to gain a deeper insight into the reason for such activity that may be associated with changes in the physical conditions of jet, such as the injection rate, Doppler factor, magnetic field strength (e.g. Böttcher & Chiang 2002; Graff et al. 2008; Hu et al. 2015, 2020), and/or the change in the acceleration process (Yan et al. 2013).

3.2.1 Locations of the radiation region

Our results show that the locations of emission regions $R_{\rm loc}$ can only be constrained well for the data of 3C 454.3 on December 2 and 3 (see Figs A1, A2 and A4 in Appendix A). It can be found from Table 1 that the marginalized 95 per cent confidence intervals (CIs) of $R_{\rm loc}$ in logarithmic space are [17.88–18.12] cm and [17.95–18.52] cm, respectively. This agrees with the result derived by Nalewajko, Begelman & Sikora (2014) who used an independent method to constrain the γ-ray emission site. For the other states of 3C 454.3 and 3C 279, a meaningful constraint on $R_{\rm loc}$ cannot be obtained, and the 95 per cent lower limits are reported in Table 1. Note that an upper limit, $R_{\rm loc} \leq R_{\rm DT} = 2.5 \times 10^{18} L_{\rm d,45}^{1/2}$, can be imposed by the adopted DT geometry. Using the vales of $L_{\rm d}$ obtained from observations, we have $R_{\rm DT} \simeq 1.36 \times 10^{19}$ cm for 3C 454.3.

3.2.2 Magnetic field strength and Doppler factor

The magnetic field strength B' and the Doppler factor $\delta_{\rm D}$ are well constrained (see Figs A1–A4 in Appendix A).

The value of B' is $\sim$1 G in all states for 3C 454.3 and 3C 279, and it varies in the range of [0.03, 0.1] G for Mrk 421. This is in agreement with the value deduced from the modelling of SEDs presented in previous studies (e.g. Yan et al. 2013; Böttcher & Baring 2019; Hu et al. 2020). However, the values of B' are more or less similar to that in the pc-scale jet as estimated from the core-shift measurement (Pushkarev, Hovatta & Kovalev 2012; Kutkin et al. 2014; Mohan et al. 2015). This implies that the γ-ray emission regions may be located at the pc-scale.

$\delta_{\rm D}$ is found to be larger than 30. The high value of $\delta_{\rm D}$ is are roughly consistent with that estimated from the radio variability time-scales (Hovatta et al. 2009). Moreover, it is also supported by the studies of the kinematics of the jet of 3C 279 (Lister & Marscher 1997; Jorstad et al. 2004) and 3C 454.3 (Lister et al. 2009; Jorstad et al. 2010, 2013). For Mrk 421, the high values of $\delta_{\rm D}$ are consistent with the results reported in Hervet et al. (2019). Note that $\delta_{\rm D}$ for Mrk 421 is generally larger than that for 3C 454.3 and 3C 279.

3.2.3 Injection electron spectrum

We find that the parameters of the injection electron spectrum, i.e. $L'_{\rm inj}$, $\gamma'_{\rm min}$ and n, are constrained very well for all SEDs (see Figs A1–A4 in Appendix A). From Table 1, it can be seen that the power-law indices of the injection electron spectrum are restricted to relatively small ranges: $n \simeq 2.0-2.3$ for Mrk 421, 3.0−3.3 for 3C 454.3 and 3.1−3.7 for 3C 279.

For the FSRQs, $L'_{\rm inj}$ varies from $\sim 7 \times 10^{41}$ to 2×10^{43} erg s^{-1}, and it is $\sim 5 \times 10^{39}$ erg s^{-1} for Mrk 421. In the L_γ–$L'_{\rm inj}$ plot, we find that the powers of injected electrons $L'_{\rm inj}$ increase with L_γ in 3C 454.3 and 3C 279. For the three sources, the best linear fit in log scale gives $L'_{\rm inj} \propto L_\gamma^{0.86\pm0.03}$ with a Pearson correlation coefficient of $r = 0.99$ and a chance probability of $p = 4.66 \times 10^{-11}$.

Table 2. Mean values and 1σ errors of the derived parameters for 3C 454.3, Mrk 421 and 3C 279. Columns 1–4 show the jet power carried by the magnetic field, electrons, cold protons and radiation, respectively. All the values are in logarithmic space. Column 5 gives the equipartition parameter and Column 6 gives the magnetization parameter. The † symbol denotes that the results were obtained with $t_{\rm var} = 1$ d.

State	$\log_{10}P_B$ (1)	$\log_{10}P_{\rm e}$ (2)	$\log_{10}P_{\rm p}$ (3)	$\log_{10}P_{\rm r}$ (4)	$U'_B/U'_{\rm e}\,(10^{-1})$ (5)	$\sigma_{\rm m}\,(10^{-2})$ (6)
3C 454.3						
Low	44.56 ± 0.27	45.24 ± 0.06	46.58 ± 0.06	44.88 ± 0.03	2.85 ± 2.84	2.22 ± 1.43
Low†	44.92 ± 0.22	45.35 ± 0.02	46.75 ± 0.07	45.19 ± 0.03	4.27 ± 2.46	3.18 ± 1.34
Nov 06	44.90 ± 0.26	45.68 ± 0.05	47.21 ± 0.06	45.31 ± 0.03	2.13 ± 1.55	1.14 ± 0.60
Nov 27	44.33 ± 0.26	45.90 ± 0.04	47.28 ± 0.07	45.80 ± 0.06	0.35 ± 0.32	0.25 ± 0.15
Dec 01	44.86 ± 0.18	45.94 ± 0.03	47.48 ± 0.05	45.79 ± 0.03	0.92 ± 0.49	0.51 ± 0.18
Dec 02	45.63 ± 0.25	46.11 ± 0.07	48.10 ± 0.13	45.98 ± 0.03	4.00 ± 2.52	0.76 ± 0.38
Dec 03	44.91 ± 0.16	46.01 ± 0.02	47.64 ± 0.06	45.92 ± 0.02	0.86 ± 0.33	0.38 ± 0.09
Mrk 421						
Quiet	42.23 ± 0.03	43.88 ± 0.04	43.90 ± 0.04	41.59 ± 0.04	0.23 ± 0.04	4.33 ± 0.65
Quiet†	42.83 ± 0.03	43.89 ± 0.04	43.68 ± 0.04	42.40 ± 0.03	0.88 ± 0.13	28.69 ± 3.75
55266	42.07 ± 0.08	44.01 ± 0.09	43.93 ± 0.06	41.78 ± 0.08	0.12 ± 0.05	2.90 ± 0.90
55270	42.23 ± 0.08	43.84 ± 0.09	43.88 ± 0.06	41.79 ± 0.08	0.26 ± 0.10	4.64 ± 1.44
55277	42.46 ± 0.14	43.56 ± 0.17	43.75 ± 0.09	41.80 ± 0.17	0.98 ± 0.53	11.62 ± 4.79
3C 279						
Period A	44.39 ± 0.06	44.98 ± 0.02	46.31 ± 0.03	44.31 ± 0.03	2.63 ± 0.39	2.39 ± 0.26
Period A†	45.47 ± 0.11	45.12 ± 0.02	46.77 ± 0.05	44.87 ± 0.02	23.07 ± 6.19	10.09 ± 1.82
Period C	44.35 ± 0.05	45.16 ± 0.02	46.50 ± 0.03	44.59 ± 0.03	1.56 ± 0.23	1.43 ± 0.17
Period D	43.82 ± 0.14	45.47 ± 0.04	46.72 ± 0.05	45.18 ± 0.04	0.24 ± 0.11	0.26 ± 0.07

Our results show that $\gamma'_{\rm min}$ is in the range of [340, 740] for Mrk 421, and it is in the range of $[400, 10^3]$ for the two FSRQs. Moreover, we note that $\gamma'_{\rm min}$ increases with L_γ in 3C 279 (Hu et al. 2020), and there are no such a trend in 3C 454.3 and Mrk 421. Notice that for the two FSRQs $\gamma'_{\rm min}$ is in the fast-cooling regime, while for Mrk 421 it is in the slow-cooling regime.

3.2.4 *Jet powers*

We evaluate the powers of the relativistic jet from our spectral fits. To consider the uncertainties on the transport parameters, we obtain the values of the derived parameters by using the MCMC code adopted. In the right panels of Figs A1–A4 in Appendix A, we display the corner plots of the derived parameters, and the mean values and 1σ uncertainties are listed in Table 2.

Assuming that there is one proton per radiating electron, the jet powers carried by the magnetic field P_B, relativistic electrons $P_{\rm e}$ and protons $P_{\rm p}$, as well as radiation $P_{\rm r}$, are evaluated through the method implemented by Celotti & Fabian (1993).

The jet powers of FSRQs 3C 454.3 and 3C 279 are significantly larger than that of HBL Mrk 421. Further, we find $P_{\rm p} \simeq P_e > P_B > P_{\rm r}$ for Mrk 421, and $P_{\rm p} > P_{\rm e} > P_{\rm r} \gtrsim P_B$ for 3C 454.3 and 3C 279, respectively. This generally agrees with previous works for BL Lacs (e.g. Zhang et al. 2012; Yan et al. 2014) and FSRQs (e.g. Celotti & Ghisellini 2008; Ghisellini et al. 2010; Ghisellini & Tavecchio 2015).

3.2.5 *Equipartition and magnetization*

Using our modelling results, we can obtain the equipartition parameter $U'_B/U'_{\rm e}$, where U'_B and $U'_{\rm e}$ are, respectively, the magnetic field and relativistic electrons energy densities in the rest frame of the jet. In addition, we calculate the magnetization parameter,[2] $\sigma_{\rm m} \equiv (\upsilon_{\rm A}/c)^2$ (Cerutti et al. 2012; Sironi et al. 2013; Sironi & Spitkovsky 2014), where $\upsilon_{\rm A}$ is equal to $B'/\sqrt{4\pi n_{\rm p} m_{\rm p}}$, with $n_{\rm p}$ and $m_{\rm p}$ denoting the thermal proton number density and rest mass, respectively.

The variations of the equipartition ($U'_B/U'_{\rm e}$) and magnetization ($\sigma_{\rm m}$) with activities are shown in Fig. 5, with the values summarized in Table 2. $U'_B/U'_{\rm e}$ ranges from 0.01 to 0.3, deviating from equipartition. No difference is found between the values for HBLs and FSRQs. $U'_B/U'_{\rm e}$ is not correlated with L_γ.

With a large sample of γ-ray blazars, Chen (2018) found that the equipartition parameter of blazars has a large width in its distribution, and that BL Lacs have much smaller $U'_B/U'_{\rm e}$, compared with FSRQs.

$\sigma_{\rm m}$ is in the range of 0.002–0.1. Mrk 421 has larger $\sigma_{\rm m}$ than that of 3C 454.3 and 3C 279. $\sigma_{\rm m}$ varies from 0.03 to 0.2 for Mrk 421, which is in good agreement with the results of Lewis et al. (2016) obtained by comparing the theoretical model with the X-ray time lags during the 1998 April 21 flare. In particular, using a relativistic oblique shock acceleration + radiation-transfer model, Böttcher & Baring (2019) successfully explained the SEDs and variabilities of 3C 279 during the flaring activity considered in the work. They obtained the non-relativistic magnetization $\sigma = 3.42$ in period A and 1.84 in period C. Using the relation $\sigma_{\rm m} = \sigma\Gamma_{\rm sh}/(m_{\rm p}/m_{\rm e})$ and $\Gamma_{\rm sh} = \delta_{\rm D}$, we obtain $\sigma_{\rm m} = 6.9 \times 10^{-2}$ and 3.9×10^{-2}, respectively. These values are also in good agreement with our results.

There is a good correlation between $\sigma_{\rm m}$ and L_γ. We obtain $\sigma_{\rm m} \propto L_\gamma^{-0.22\pm0.04}$ with a Pearson correlation coefficient of $r = -0.86$ and a chance of probability of $p = 1.61 \times 10^{-4}$.

[2]Note that the definition of $\sigma_{\rm m}$ can be related to the non-relativistic magnetization defined by Baring, Böttcher & Summerlin (2017), through the relation $\sigma_{\rm m} = \sigma\Gamma_{\rm sh}/(m_{\rm p}/m_{\rm e})$. However, the definition of $\sigma_{\rm m}$ may be equivalent to the definition of $\sigma \equiv P_B/P_m$, where $P_{\rm m} = P_{\rm e} + P_{\rm p}$ is the kinetic power of matter. For Mrk 421, we can obtain $\sigma_{\rm m} \simeq P_B/P_{\rm p} \simeq P_B/P_{\rm e}$, because $P_{\rm e} \sim P_{\rm p}$. For 3C 454.3 and 3C 279, we can obtain $\sigma_{\rm m} \simeq 2P_B/P_{\rm p}$, as $P_{\rm p} \gg P_{\rm e}$.

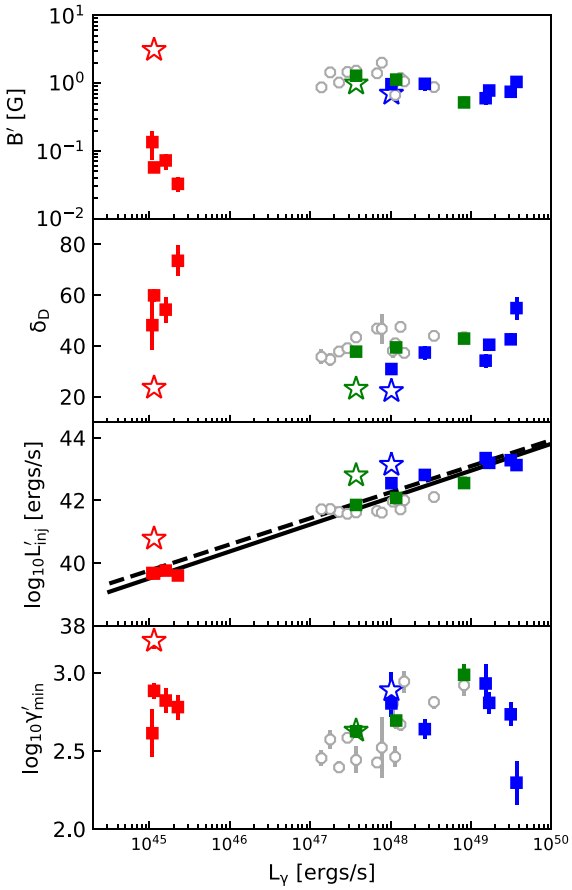

Figure 4. Evolution of the model parameters as a function of the observed γ-ray luminosity. The red, blue and green squares are the results of Mrk 421, 3C 454.3 and 3C 279, respectively. The open stars denote the results obtained with $t_{\rm var} = 1$ d for the quiescent states of the three sources. For 3C 279, the model parameters reported in Hu et al. (2020) are also shown in each panel, and are denoted by the grey open circles. In the L_γ–$L'_{\rm inj}$ plot, the solid and dashed lines denote the best linear fits to the results with a short- and long-variability time-scale for the quiescent states, respectively.

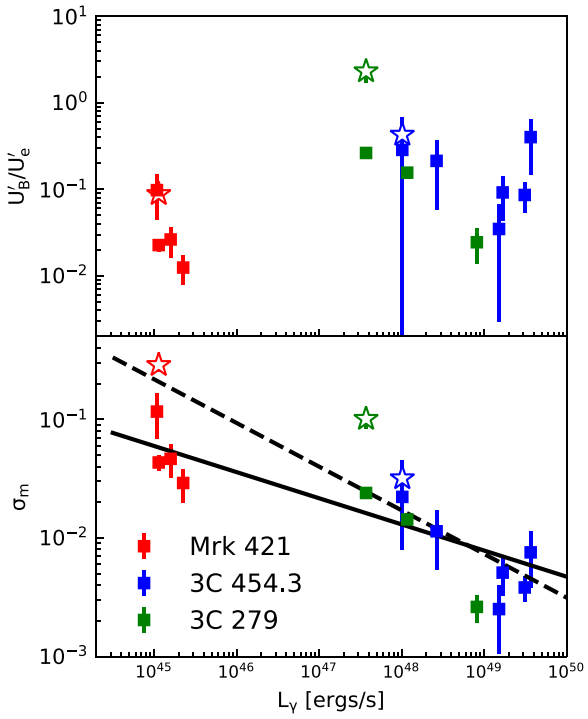

Figure 5. Evolution of the equipartition (upper) and magnetization (lower) parameters as a function of the observed γ-ray luminosity. The open stars denote the results derived with $t_{\rm var} = 1$ d for the quiescent states of the three sources. In the L_γ–$\sigma_{\rm m}$ plot, the solid and dashed lines denote the best linear fits to the results with a short- and long-variability time-scale for the quiescent states, respectively.

4 DISCUSSION AND CONCLUSIONS

Using a single-zone leptonic model and the MCMC fitting technique, we model the high-quality and simultaneous MWL SEDs at multiple epochs of three typical blazars (3C 454.3, 3C 279 and Mrk 421). For 3C 454.3, the SEDs in a low γ-ray state and the five highest γ-ray flaring states (Bonnoli et al. 2011) are considered. For Mrk 421, we consider the SED in a γ-ray quiescent state (Abdo et al. 2011b) and the SEDs in three highest γ-ray flaring states reported in Aleksić et al. (2015). For 3C 279, we consider three SEDs in Hayashida et al. (2015), which are the representatives for the 14 SEDs studied in Hu et al. (2020). The jet model used here is a refined model of Hu et al. (2020).

We find that the model can explain the SEDs well. The properties of the emission regions obtained by using our model are consistent with previous studies. Mrk 421 has smaller magnetic field strength and larger Doppler factor than 3C 454.3 and 3C 279. The electron injection spectrum of 3C 279 and 3C 454.3 is steeper than that of Mrk 421. Mrk 421 has smaller electron injection power and larger magnetization than 3C 454.3 and 3C 279. The three jets are found to be low-magnetization and non-equipartition, suggesting that electrons can be accelerated by shock in the jet.

The new findings are the tight correlations between L_γ and $L'_{\rm inj}$, $\sigma_{\rm m}$. The correlation between L_γ and $L'_{\rm inj}$ has been found when modelling the 14 SEDs of 3C 279 (Hu et al. 2020). Here, after including the HBL Mrk 421 and 3C 454.3, this relation still holds. $L'_{\rm inj}$ can be associated with acceleration in the jet. The correlation between L_γ and $L'_{\rm inj}$ suggests that the particle acceleration process plays an important role in driving the γ-ray flares of blazars.

As mentioned above, the low magnetization ($\sigma_{\rm m} \leq 0.1$) indicates that shocks might be responsible for the acceleration of the electrons in the jets (e.g. Sironi et al. 2015). The anticorrelation between L_γ and $\sigma_{\rm m}$ is first found when modelling the SEDs of blazars. This suggests that the same energy-dissipative mechanism behind the jet emission could be at work in different types of blazars.

In the above modelling, we used the minimum variability time-scale measured from the γ-ray flares for each source. The same variability time-scale is adopted for the SED in the quiescent state. This implies that the γ-rays in quiescent states and flaring states are produced in the same region. Alternatively, γ-rays in different states can be produced in different regions (e.g. Brown 2013; Coogan, Brown & Chadwick 2016; Acharyya, Chadwick & Brown 2021). In this case, a longer variability time-scale should be used for the quiescent state. In order to investigate this scenario, we also performed the fitting to the SED at the quiescent state for each source using $t_{\rm var} = 1$ d. The modelling results are shown in Fig. B1, and the corresponding corner plots of the input and output parameters are shown in Fig. B2, with the parameter values reported in Tables 1 and 2. We find that an increase of $t_{\rm var}$ could primarily lead to a decrease in $\delta_{\rm D}$ and an increase in $L'_{\rm inj}$. Also, B', $\gamma'_{\rm min}$, n and $R_{\rm loc}$ are found to change slightly. For comparison, the parameter values are

plotted in Figs 4 and 5 (open stars). Interestingly, it is found that the correlation between $L'_{\rm inj}$ and L_γ is still significant, with $r = 0.91$ and $p = 1.57 \times 10^{-5}$. In the $\sigma_{\rm m} - L_\gamma$ panel of Fig. 5, the Pearson test also gives a significant correlation with $r = -0.87$ and $p = 1.05 \times 10^{-4}$. The results could indicate that the correlations are independent of the location of the γ-ray emission region.

The variability may be caused by changes in the physical condition of the jet, such as injection, magnetic field and Doppler factor (Diltz & Böttcher 2014), with the possible intervention of shock waves or turbulence (e.g. Sikora et al. 2001; Marscher 2014). In the frame of the one-zone leptonic model, our results indicate that the electron injection may be the main driver of the variability. In other words, the acceleration of electrons causes the γ-ray variability.

In addition to the intrinsic origin of the variability, it could also be attributed to a geometrical effect of changing in the viewing angle (Raiteri et al. 2009, 2017; Villata et al. 2007; Liodakis et al. 2020). It is interesting to make a distinction between two explanations of variability. However, it is difficult to make such a distinction based on the current observations.

It should be pointed out that the collimation parameter of the emitting region $\Gamma\theta_{\rm obs} = 1$ is fixed in the fitting. This assumption is frequently adopted in blazar SED modelling (e.g. Zhang et al. 2012; Böttcher et al. 2013; Yan et al. 2014, 2015; Nalewajko, Begelman & Sikora 2014). However, the very-long-baseline interferometry (VLBI) observations indicate that $\Gamma\theta_{\rm obs} \ll 1$ (e.g. Jorstad et al. 2017) for some blazars. This assumption should not affect significantly the spectral fits to the observed SEDs, and it has little effect on our main conclusions. This is mainly because the emitting EEDs and the resulting SEDs are directly related to $\delta_{\rm D}$, which can remain constant by decreasing Γ and $\theta_{\rm obs}$.[3] However, we would like to emphasize that the decrease of $\Gamma\theta_{\rm obs}$ will reduce the intrinsic jet power. Therefore, it should be considered with caution when the jet powers from the spectral fitting are compared with the powers predicted by the Blanford–Payne (BP; Blandford & Payne 1982) or Blanford–Znajek (BZ; Blandford & Znajek 1977) mechanisms.

From Table 2, we can see that the averaged jet powers estimated from the SED fittings are 4.14×10^{47}, 3.74×10^{46} and 1.48×10^{44} erg s^{-1} for 3C 454.3, 3C 279 and Mrk 421, respectively. However, the jet powers can also be estimated by modelling the observed SEDs with hadronic models (e.g. Böttcher et al. 2013; Petropoulou & Dermer 2016; Barkov, Aharonian & Bosch-Ramon 2010). In particular, the hadronic models have received much attention since the detection of coincident neutrinos and γ-rays from blazar TXS 0506+056 (Aartsen et al. 2018a,b; Xue et al. 2019; 2021). The required power in relativistic protons $L_{\rm p}$ is of the order of magnitude of 10^{49} erg s^{-1} for 3C 454.3 and 10^{48} erg s^{-1} for 3C 279 (Böttcher et al. 2013), while for Mrk 421 $L_{\rm p}$ ranges from 2.3×10^{47} to 7.8×10^{47} erg s^{-1} (Petropoulou, Coenders & Dimitrakoudis 2016). It can be seen that the jet powers estimated from hadronic models are much greater than those estimated from leptonic models.

We can compare the jet power against the power of the BZ process (Blandford & Znajek 1977), which is believed to be the plausible explanation for the jet launch. Generally, the predicted jet power can be written as $P_{\rm BZ} = \eta_{\rm j} P_{\rm acc}$, where $\eta_{\rm j}$ is the jet production efficiency, and the accretion power is $P_{\rm acc} = \dot{M}c^2$ with $\dot{M}$ denoting the mass accretion rate. As has been theoretically estimated and numerically confirmed, $\eta_{\rm j}$ in a magnetically choked accretion flow scenario can exceed unity (Tchekhovskoy, Narayan & McKinney 2010; McKinney, Tchekhovskoy & Blandford 2012), and reaches $\sim$1.9 for maximal BH spins (Sikora & Begelman 2013). In FSRQs, the accretion powers can be calculated as $P_{\rm acc} = L_{\rm d}/\eta_{\rm d}$, where $\eta_{\rm d}$ is the accretion disc's radiative efficiency. Assuming $\eta_{\rm d} = 0.1$ and 0.3 (Ghisellini et al. 2014), we find that $P_{acc} \simeq (1 - 3) \times 10^{47}$ erg s^{-1} for 3C 454.3, and $P_{\rm acc} \simeq (0.67 - 2) \times 10^{46}$ erg s^{-1} for 3C 279. Compared with FSRQs, BL Lacs are believed to have low accretion rates (e.g. Wang, Staubert & Ho 2002; Xu, Cao & Wu 2009). For Mrk 421, we estimate the accretion power through the relation $P_{\rm acc} = \dot{m} L_{\rm Edd} \simeq 1.26 \times 10^{46} \dot{m} M_8$ erg s^{-1}, where $L_{\rm Edd}$ is the Eddington luminosity, $\dot{m}$ is the mass accretion rate in units of $\dot{M}_{\rm Edd} = L_{\rm Edd}/c^2$, and M_8 is the BH mass in units of 10^8 M$_\odot$. Assuming $\dot{m} \sim (3 - 10) \times 10^{-3}$ (Ghisellini & Tavecchio 2008; Meyer et al. 2011), we obtain $P_{\rm acc} \simeq (0.72 - 2.4) \times 10^{44}$ erg s^{-1} for Mrk 421, when we take $\log M_{\rm BH}/{\rm M}_\odot = 8.28$ derived from the measurement of stellar velocity dispersion (Woo & Urry 2002). Therefore, it seems that the relativistic jets in the three sources may be governed by the BZ process.

Our results show that the energy density ratio of the magnetic field and radiating electrons $U'_B/U'_{\rm e}$ varies from $\sim$0.01 to $\sim$0.5. This is consistent with results from modelling the SEDs of the large sample blazars (e.g. Celotti & Ghisellini 2008; Ghisellini et al. 2014; Chen 2018) or individual sources (e.g. Yan et al. 2013; Dermer et al. 2014; Hu et al. 2015). Interestingly, we note that in the quiescent states of the three sources $U'_B/U'_{\rm e}$ is closer to equipartition compared with the flaring states. In fact, the results may be supported by radio observations. The studies of the core-shift effect have shown that the distance of the core from the jet base $r_{\rm c}$, the core size W and the light-curve time lag Δt all depend on the observation frequency ν as $r_{\rm c} \propto W \propto \Delta t \propto \nu^{-1/k}$ with $k \simeq 1$ (e.g. Sokolovsky et al. 2011; Pushkarev et al. 2012; Zamaninasab et al. 2014; Mohan et al. 2015; Agarwal et al. 2017). This is in agreement with the prediction of a synchrotron self-absorbed conical jet model of Blandford & Königl (1979) and Königl (1981) in the case of equipartition. Plavin, Kovalev & Pushkarev (2019) argued that any fixed frequency dependence such as $r_{\rm c} \propto \nu^{-1}$ is disrupted during flares. They concluded that the observed flux density variability and the variations of the core position in a flaring jet are mainly caused by a significant increase in emitting electron density and a slight decrease in the magnetic field. This indicates that the electron energy density dominates over magnetic field energy density during flaring activity. Moreover, the extreme brightness temperatures $\geq 10^{13}$ K observed by RadioAstron also support that equipartition may be violated during flares (e.g. Gómez et al. 2016; Bruni et al. 2017; Pilipenko et al. 2018; Kutkin et al. 2018).

ACKNOWLEDGEMENTS

We thank the reviewer for constructive suggestions and comments. We acknowledge the National Natural Science Foundation of China (NSFC-11803081, NSFC-12065011,NSFC-U1831124) and the joint foundation of Department of Science and Technology of Yunnan Province and Yunnan University [2018FY001(-003)]. The work of D. H. Yan is also supported by the CAS Youth Innovation Promotion Association and Basic research Program of Yunnan Province (202001AW070013).

DATA AVAILABILITY

No new data were generated or analysed in support of this research.

[3]In the limit $\Gamma \gg 1$, $\theta_{\rm obs} \ll 1$, the Doppler factor $\delta_{\rm D}$ can be related to Γ through the relationship $\delta_{\rm D} = 2\Gamma/(1 + \Gamma^2\theta^2_{\rm obs})$ (Dermer et al. 2014).

REFERENCES

Aartsen M. G. et al., 2018a, Sci, 361, eaat1378
Aartsen M. G. et al., 2018b, Sci, 361, 147
Abdo A. A. et al., 2009, ApJ, 699, 817
Abdo A. A. et al., 2011a, ApJ, 733, L26
Abdo A. A. et al., 2011b, ApJ, 736, 131
Abeysekara A. U. et al., 2018, ApJ, 856, 95
Acharyya A., Chadwick P. M., Brown A. M., 2021, MNRAS, 500, 5297
Agarwal A. et al., 2017, MNRAS, 469, 813
Aleksić J. et al., 2015, A&A, 578, A22
Baring M. G., Böttcher M., Summerlin E. J., 2017, MNRAS, 464, 4875
Barkov M. V., Aharonian F. A., Bosch-Ramon V., 2010, ApJ, 724, 1517
Bennett C. L. et al., 2013, ApJS, 208, 20
Blandford R. D., Königl A., 1979, ApJ, 232, 34
Blandford R. D., Payne D. G., 1982, MNRAS, 199, 883
Blandford R. D., Znajek R. L., 1977, MNRAS, 179, 433
Blazejowski M., Sikora M., Moderski R., Madejski G. M., 2000, ApJ, 545, 107
Bloom S. D., Marscher A. P., 1996, ApJ, 461, 657
Blumenthal G. R., Gould R. J., 1970, Rev. Mod. Phys., 42, 237
Bonnoli G., Ghisellini G., Foschini L., Tavecchio F., Ghirlanda G., 2011, MNRAS, 410, 368
Brown A. M., 2013, MNRAS, 431, 824B
Bruni G. et al., 2017, A&A, 604, A111
Böttcher M., Baring M. G., 2019, ApJ, 887, 133
Böttcher M., Chiang J., 2002, ApJ, 581, 127
Böttcher M., Reimer A., Sweeney K., Prakash A., 2013, ApJ, 768, 54
Celotti A., Fabian A. C., 1993, MNRAS, 264, 228
Celotti A., Ghisellini G., 2008, MNRAS, 385, 283
Cerutti B., Uzdensky D. A., Begelman M. C., 2012, ApJ, 746, 148
Chen L., 2018, ApJ, 235, 39
Chiaberge M., Ghisellini G., 1999, MNRAS, 306, 551
Christie I. M., Petropoulou M., Sironi L., Giannios D., 2019, MNRAS, 482, 65
Coogan R. T., Brown A. M., Chadwick P. M., 2016, MNRAS, 458, 354C
Coppi P. S., Blandford R. D., 1990, MNRAS, 245, 453
Crusius A., Schlickeiser R., 1986, A&A, 164, L16
Dermer C. D., Cerruti M., Lott B., Boisson C., Zech A., 2014, ApJ, 782, 82
Dermer C. D., Fink J. D., Krug H., Böttcher M., 2009, ApJ, 692, 32
Dermer C. D., Schlickeiser R., 1993, ApJ, 416, 458D
Dermer C. D., Schlickeiser R., 2002, ApJ, 757, 667
Diltz C., Böttcher M., 2014, J. High Energy Astrophys., 1, 63
D'arcangelo F. D. et al., 2009, ApJ, 697, 985
Finke J. D., 2016, ApJ, 830, 94
Finke J. D., Dermer C. D., Böttcher M., 2008, ApJ, 686, 181
Ghisellini G., Tavecchio F., 2008, MNRAS, 387, 1669
Ghisellini G., Tavecchio F., 2009, MNRAS, 397, 985
Ghisellini G., Tavecchio F., 2015, MNRAS, 448, 1060
Ghisellini G., Tavecchio F., Foschini L., Ghirlanda G., Maraschi L., Celotti A., 2010, MNRAS, 402, 497
Ghisellini G., Tavecchio F., Maraschi L., Celotti A., Sbarrato T., 2014, Nature, 515, 376
Giannios D., 2013, MNRAS, 431, 355
Giannios D., Uzdensky D. A., Begelman M. C., 2009, MNRAS, 395, L29
Graff P. B., Georganopoulos M., Perlman E. S., Kazanas D., 2008, ApJ, 689, 68
Gu M., Cao X., Jiang D. R., 2001, MNRAS, 327, 1111
Guo F., Li H., Daughton W., Liu Y-H., 2014, Phys. Rev. Lett., 113, 155005
Guo F., Liu Y-H., Daughton W., Li H., 2015, ApJ, 806, 167
Gómez J. L. et al., 2016, ApJ, 817, 96
Hayashida M. et al., 2015, ApJ, 807, 79
Hervet O., Williams D. A., Falcone A. D., Kaur A., 2019, ApJ, 877, 26
Hinshaw G. et al., 2013, ApJS, 208, 19
Homan D. C., Kadler M., Kellermann K. I., Kovalev Y. Y., Lister M. L., Ros E., Savolainen T., Zensus J. A., 2009, ApJ, 706, 1253
Hovatta T., Valtaoja E., Tornikoski M., Lähteenmäki A., 2009, A&A, 494, 527
Hu W., Dai B-Z, Zeng W., Fan Z-H, Zhang L., 2017, New Astron., 52, 82
Hu W., Fan Z-H., Dai B-Z., 2015, Res. Astron. Astrophys., 15, 1455
Hu W., Yan D. H., Dai B-Z, Zeng W., Hu Q. L., 2020, MNRAS, 493, 410
Inoue Y., Tanaka Y. T., 2016, ApJ, 828, 13
Jackson N., Browne W. A., 1991, MNRAS, 250, 414
Jones F. C., 1968, Phys. Rev., 167, 1159J
Jorstad S. G., Marscher A. P., Lister M. L., Stirling A. M., Cawthorne T. V., Gómez J.-L., Gear W. K., 2004, AJ, 127, 3115
Jorstad S. G. et al., 2005, AJ, 130, 1418
Jorstad S. G. et al., 2010, ApJ, 715, 362
Jorstad S. G. et al., 2013, ApJ, 773, 147
Jorstad S. G. et al., 2017, ApJ, 846, 98
Kirk J. G., Guthmann A. W., Gallant Y. A., Achterberg A., 2000, ApJ, 542, 235
Kutkin A. M. et al., 2014, MNRAS, 437, 3396
Kutkin A. M. et al., 2018, MNRAS, 475, 4994
Königl A., 1981, ApJ, 243, 700
Lewis A., Bridle S., 2002, Phys. Rev. D, 66, 103511
Lewis T. R., Becker P. A., Finke J. D., 2016, ApJ, 824, 108
Lewis T. R., Finke J. D., Becker P. A., 2018, ApJ, 853, 6
Liodakis I. et al., 2020, ApJ, 902, 61
Lister M. L., Marscher A. P., 1997, ApJ, 476, 572
Lister M. L. et al., 2009, AJ, 138, 1874
Liu J., Yuan Q., Bi X. J., Li H., Zhang X. M., 2012, Phys. Rev. D, 85, d3507
Marscher A. P., 2014, ApJ, 780, 87
Marscher A. P., Gear W. K., 1985, ApJ, 298, 114
Marscher A. P. et al., 2008, Nature, 452, 966
Marscher A. P. et al., 2010, ApJ, 710, L126
McKinney J. C., Tchekhovskoy A., Blandford R. D., 2012, MNRAS, 423, 3083
Meyer E. T., Fossati G., Georganopoulos M., Lister M. L., 2011, ApJ, 740, 98
Mohan P. et al., 2015, MNRAS, 452, 2004
Nalewajko K., Begelman M. C., Sikora M., 2014, ApJ, 789, 161
Nilsson K., Pursimo T., Villforth C., Lindfors E., Takalo L. O., 2009, A&A, 505, 601
Peceur N. M., Tayler A. R., Kraan-Korteweg R. C., 2020, MNRAS, 495, 2162
Petropoulou M., Coenders S., Dimitrakoudis S., 2016, Astropart. Phys., 80, 115
Petropoulou M., Dermer C. D., 2016, ApJ, 825, L11
Petropoulou M., Giannios D., Sironi L., 2016, MNRAS, 462, 3325
Petropoulou M., Sironi L., Spitkovsky A., Giannios D., 2019, ApJ, 880, 37
Pian E. et al., 1999, ApJ, 521, 112
Pilipenko S. V. et al., 2018, MNRAS, 474, 3523
Plavin A. V., Kovalev Y. Y., Pushkarev A. B., 2019, MNRAS, 485, 1822
Poole T. S. et al., 2008, MNRAS, 383, 627
Punch M. et al., 1992, Nature, 358, 477
Pushkarev A. B., Hovatta T., Kovalev Y. Y., 2012, A&A, 545, A113
Raiteri C. M. et al., 2007, A&A, 473, 819
Raiteri C. M. et al., 2008, A&A, 485, L17
Raiteri C. M. et al., 2009, A&A, 507, 769
Raiteri C. M. et al., 2017, Nature, 552, 374
Rybicki G. B., Lightman A. P., 1979, Radiative Processes in Astrophysics. Wiley, New York
Shah Z., Sahayanathan S., Mankuzhiyil N., Kushwaha P., Misra R., Iqbal N., 2017, MNRAS, 470, 3283S
Shakura N. I., Sunyaev R. A., 1973, A&A, 24, 337
Sikora M., Begelman M. C., 2013, ApJ, 764, L24
Sikora M., Begelman M. C., Rees M. J., 1994, ApJ, 421, 153
Sikora M., Błaz`ejowski M., Begelman M. C., Moderski R., 2001, ApJ, 554, 1
Sironi L., Petropoulou M., Giannios D., 2015, MNRAS, 450, 183
Sironi L., Spitkovsky A., 2009, ApJ, 698, 1523
Sironi L., Spitkovsky A., 2014, ApJ, 783, L21
Sironi L., Spitkovsky A., Arons J., 2013, ApJ, 771, 54
Sokolovsky K. V., Kovalev Y. Y., Pushkarev A. B., Lobanov A. P., 2011, A&A, 532, A38

Spada M., Ghisellini G., Lazzati D., Celotti A., 2001, MNRAS, 325, 1559
Summerlin E. J., Baring M. G., 2012, ApJ, 745, 63
Tavecchio F., Ghisellini G., 2008, MNRAS, 386, 945T
Tavecchio F., Ghisellini G., Bonnoli G., Ghirlanda G., 2010, MNRAS, 405, L94
Tchekhovskoy A., Narayan R., McKinney J. C., 2010, ApJ, 711, 50
Urry C. M., Padovani P., 1995, PASP, 107, 803
Vercellone S. et al., 2009, ApJ, 690, 1018
Vercellone S. et al., 2010, ApJ, 712, 405
Vercellone S. et al., 2011, ApJ, 736, L38
Villata M. et al., 2006, A&A, 453, 817
Villata M. et al., 2007, A&A, 464, L5
Wang J-M., Staubert R., Ho L. C., 2002, ApJ, 579, 554
Woo J. H., Urry C. M., 2002, ApJ, 579, 530
Wu L-H., Wu Q., Yan D-H., Chen L., Fan X., 2018, ApJ, 852, 45
Xue R., Liu R-Y., Petropoulou M., Oikonomou F., Wang Z-R., Wang K., Wang X-Y., 2019, ApJ, 886, 23X
Xue R., Liu R-Y., Wang Z-R., Ding N., Wang X-Y., 2021, ApJ, 906, 51X
Xu Y-D., Cao X., Wu Q., 2009, ApJ, 694, L107
Yan D. H., Zeng H. D., Zhang L., 2012, PASJ, 64, 80
Yan D. H., Zeng H. D., Zhang L., 2014, MNRAS, 439, 2933
Yan D. H., Zhang L., Yuan Q., Fan Z. H., Zeng H. D., 2013, ApJ, 765, 122
Yan D. H., Zhang L., Zhang S. N., 2015, MNRAS, 454, 1310
Yuan Q., Liu S., Fan Z., Bi X., Fryer C., 2011, ApJ, 735, 120
Zamaninasab M., Clausen-Brown E., Savolainen T., Tchekhovskoy A., 2014, Nature, 510, 126
Zhang J., Liang E-W., Zhang S-N., Bai J. M., 2012, ApJ, 752, 157

APPENDIX A: CORNER PLOTS OF MODEL PARAMETERS

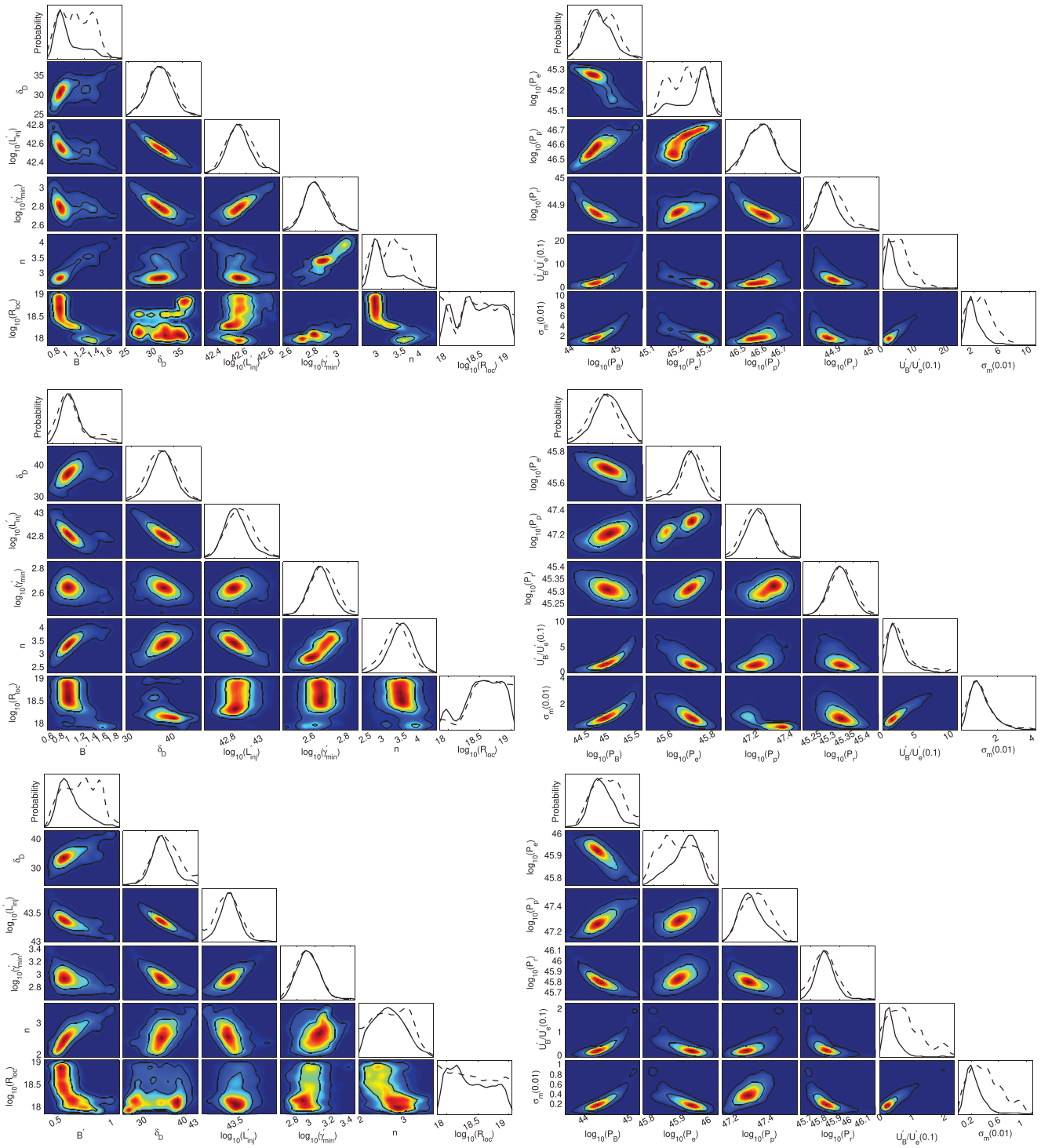

Figure A1. Corner plots of the free model parameters (left) and derived parameters (right) for FSRQs 3C 454.3. For the two-dimensional confidence contours of the parameters, the inner and outer contours denote the 68 and 95 per cent confidence intervals, respectively. For the one-dimensional probability distributions of the parameters, the dashed lines show the maximum likelihood distributions and solid lines show the marginalized probability distributions. From top to bottom, the plots are the results obtained from fitting SEDs at low γ-ray state, November 6 and 27, as reported in Bonnoli et al. (2011), respectively.

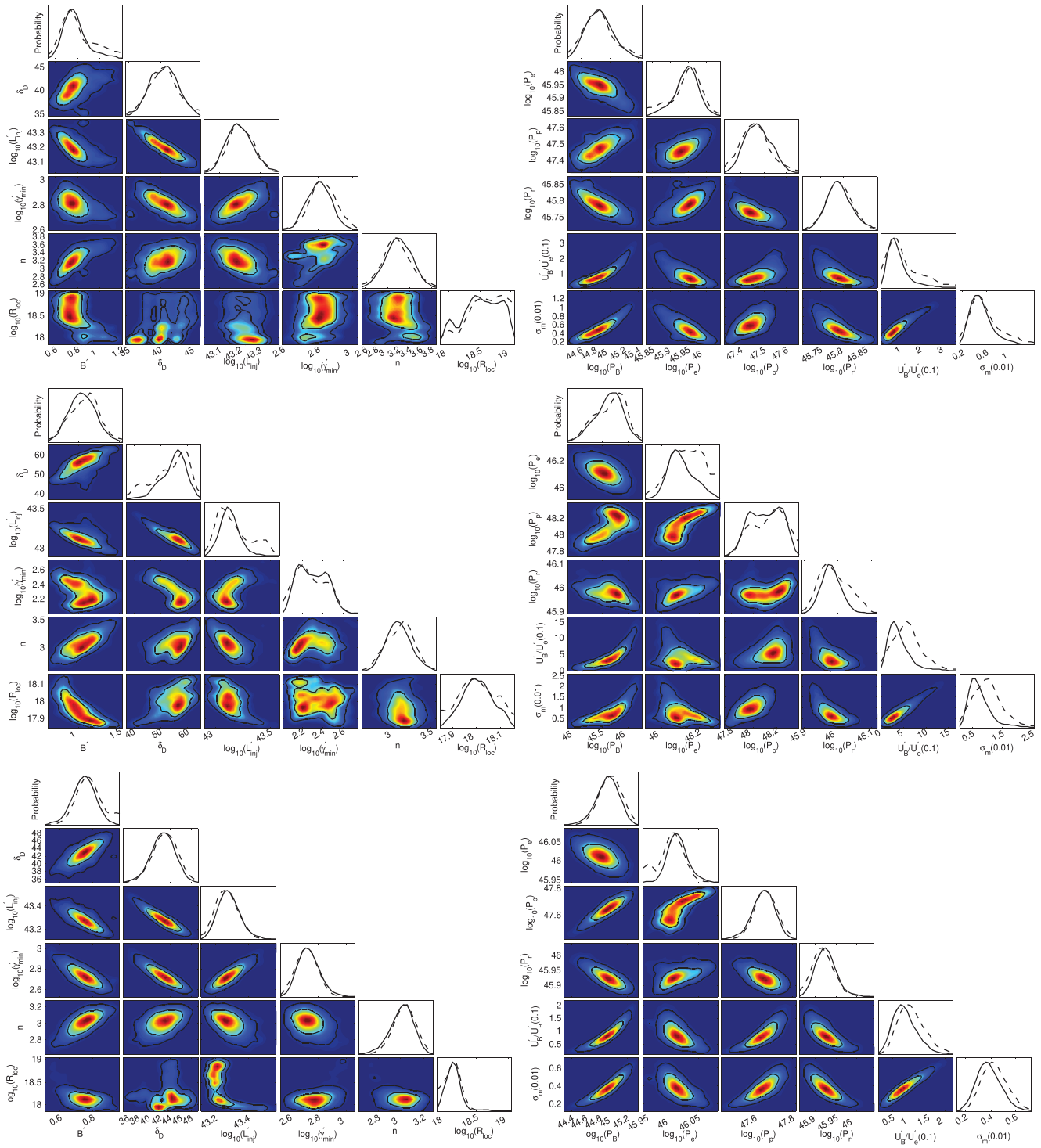

Figure A2. Same as Fig. A1, but for the SEDs on December 1 (top), December 2 (middle) and December 3 (bottom).

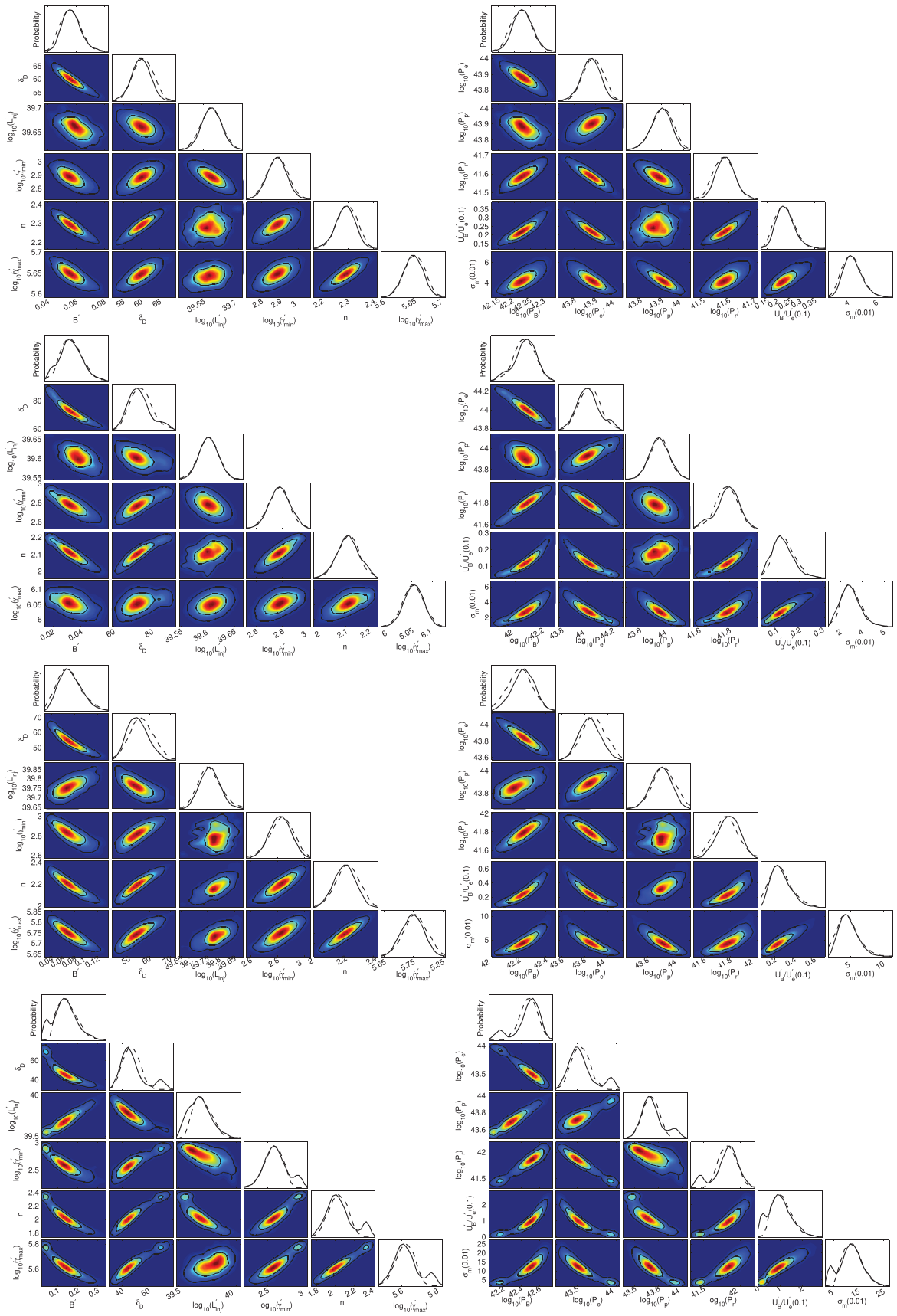

Figure A3. Corner plots of the input (left) and output parameters (right) for HBL Mrk 421. From top to bottom, the plots are arranged in the following order: quiescent state, 55266, 55270 and 55277.

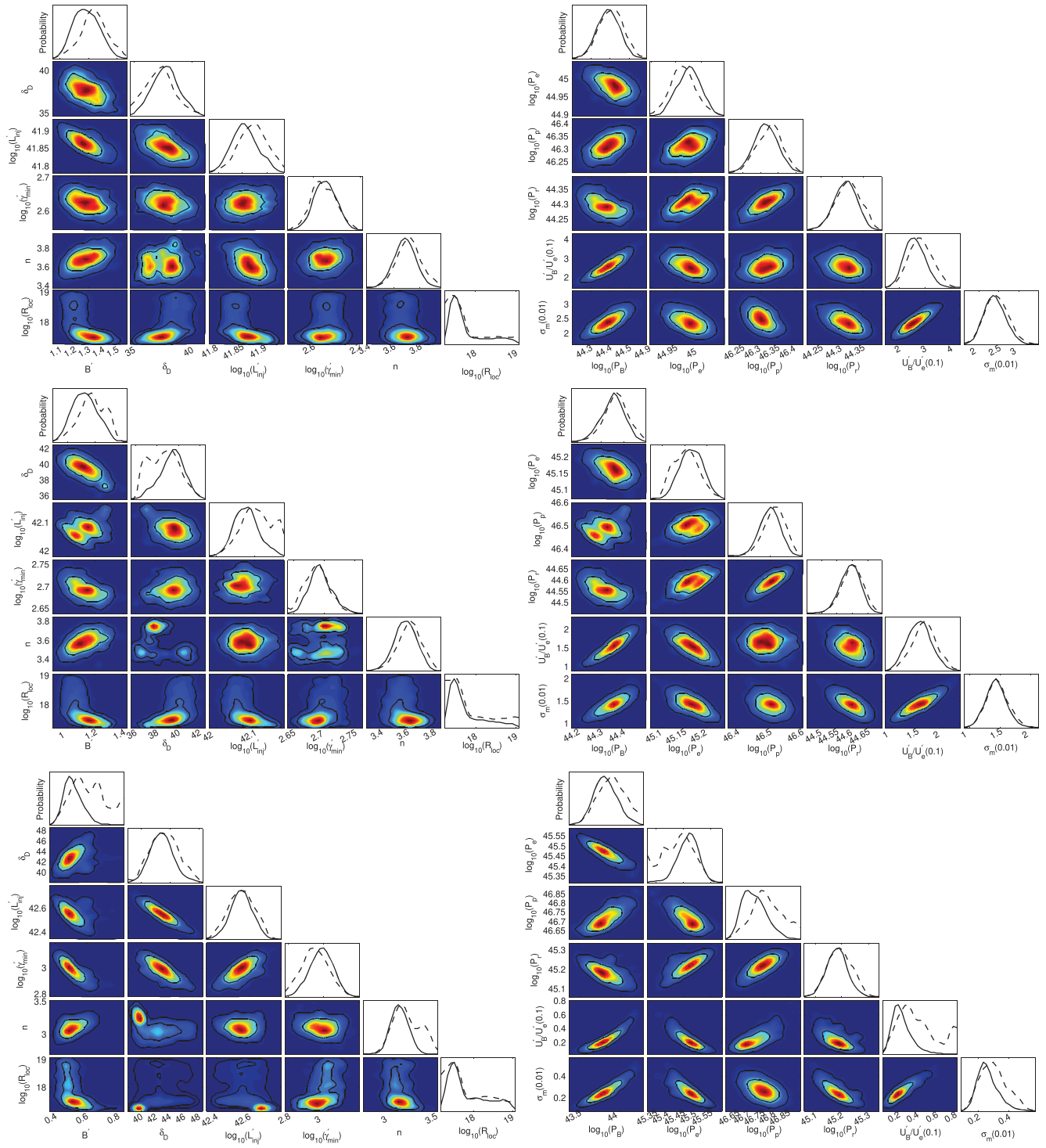

Figure A4. Corner plots of the free model parameters (left) and derived parameters (right) for FSRQs 3C 279. From top to bottom, the plots are the results obtained from fitting SEDs in Periods A, C and D reported in Hayashida et al. (2015), respectively.

APPENDIX B: SED FITTING WITH THE VARIABILITY TIME-SCALE OF ONE DAY FOR QUIESCENT STATES

Fig. B1 shows the best-fitting SEDs to the three sources at the quiescent states with $t_{\rm var} = 1$d, and Fig. B2 shows the corner plots of the model parameters. The results of this analysis are discussed in detail in Section 4, and the values are shown in Tables 1 and 2.

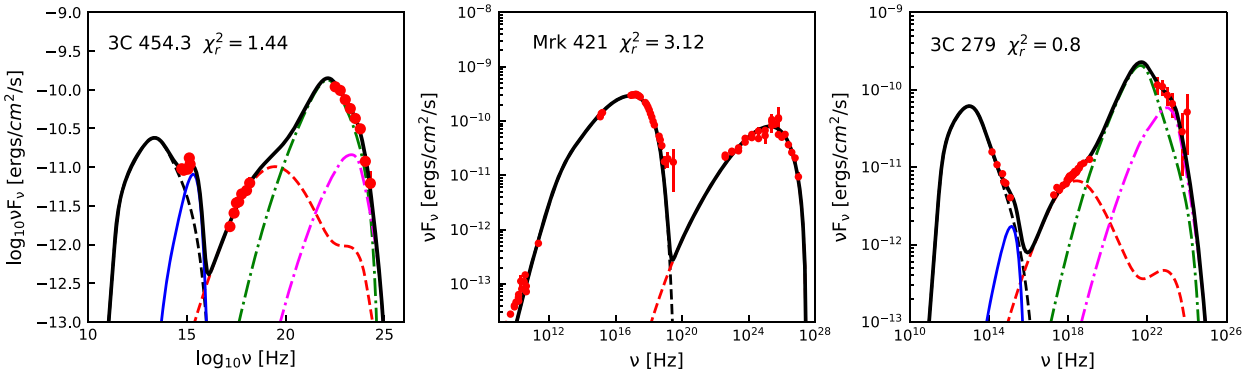

Figure B1. Comparisons of the best-fitting SEDs with observed data of 3C 454.3, Mrk 421 and 3C 279 at the quiescent states with $t_{\rm var} = 1$d.

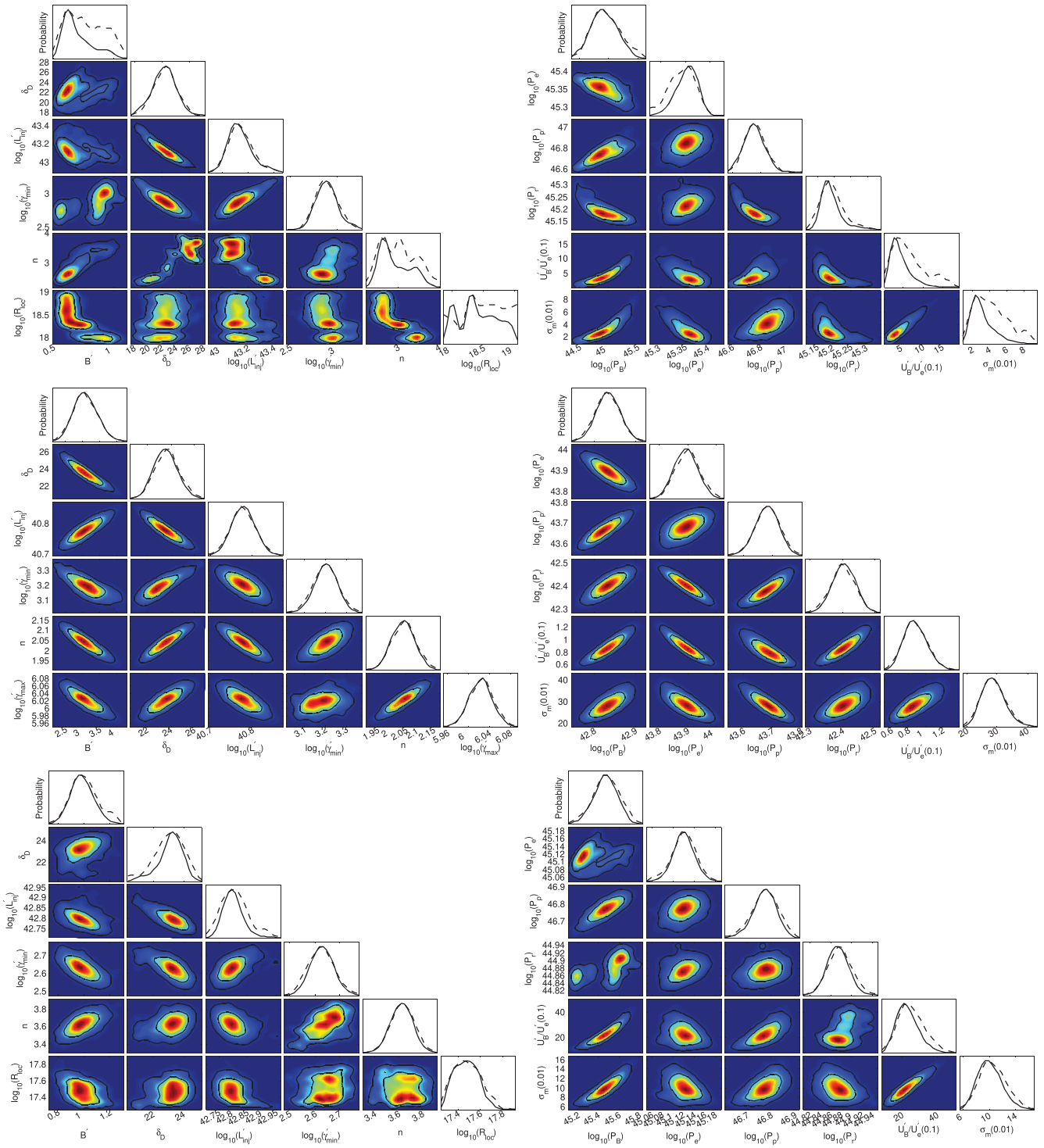

Figure B2. Corner plots of the free model parameters (left) and derived parameters (right) for the quiescent states with $t_{\rm var} = 1$d. From top to bottom, the plots are the results obtained from fitting SEDs for 3C 454.3, Mrk 421 and 3C 279, respectively.

This paper has been typeset from a TEX/LATEX file prepared by the author.